PHOTONICS Research

High-performance modified uni-traveling carrier photodiode integrated on a thin-film lithium niobate platform

Xiangwen Guo,[1] Linbo Shao,[2] Lingyan He,[3] Kevin Luke,[3] Jesse Morgan,[1] Keye Sun,[1] Junyi Gao,[1] Ta-Ching Tzu,[1] Yang Shen,[1] Dekang Chen,[1] Bingtian Guo,[1] Fengxin Yu,[1] Qianhuan Yu,[1] Masoud Jafari,[1] Marko Lončar,[2] Mian Zhang,[3] and Andreas Beling[1,*]

[1]Department of Electrical and Computer Engineering, University of Virginia, Charlottesville, Virginia 22903, USA
[2]John A. Paulson School of Engineering and Applied Sciences, Harvard University, Cambridge, Massachusetts 02138, USA
[3]HyperLight Corporation, Cambridge, Massachusetts 02139, USA
*Corresponding author: ab3pj@virginia.edu

Received 10 February 2022; revised 4 April 2022; accepted 6 April 2022; posted 7 April 2022 (Doc. ID 455969); published 12 May 2022

Lithium niobate on insulator (LNOI) has become an intriguing platform for integrated photonics for applications in communications, microwave photonics, and computing. Whereas, integrated devices including modulators, resonators, and lasers with high performance have been recently realized on the LNOI platform, high-speed photodetectors, an essential building block in photonic integrated circuits, have not been demonstrated on LNOI yet. Here, we demonstrate for the first time, heterogeneously integrated modified uni-traveling carrier photodiodes on LNOI with a record-high bandwidth of 80 GHz and a responsivity of 0.6 A/W at a 1550-nm wavelength. The photodiodes are based on an n-down InGaAs/InP epitaxial layer structure that was optimized for high carrier transit time-limited bandwidth. Photodiode integration was achieved using a scalable wafer die bonding approach that is fully compatible with the LNOI platform. © 2022 Chinese Laser Press

https://doi.org/10.1364/PRJ.455969

1. INTRODUCTION

Photonic integration holds the promise for realizing high-performance, low-cost, scalable solutions for communication, sensing, and quantum computation applications. Lithium niobate (LN) is one of the most suitable material platforms for integrated photonic circuits due to its unique material properties including the large electro-optic coefficient, the large second-order nonlinear susceptibility, and a wide optical transparency window (350 nm–5 μm) [1]. LN-based devices, such as electro-optic modulators, have been the workhorse of the optoelectronic industry for decades [2]. Recently, the revolutionary technology of lithium niobate on insulator (LNOI) and breakthroughs in nanofabrication techniques have made high-performance-integrated nanophotonic components possible and the manufacturing of wafer-scale high-quality devices on LNOI has become fully commercialized [3]. Moreover, these nanostructure devices, such as optical modulators and nonlinear wavelength converters have already outperformed legacy devices in bulk form [2]. Nanofabrication breakthroughs enabled ultra-low-loss resonators to be built on LNOI which realized novel applications, such as optical frequency combs and quantum transducers [3]. LNOI high-speed electro-optic modulators have become commercialized and work fully compatibly with complementary metal-oxide semiconductor (CMOS) voltages [2]. Lately, lasers were proven to have the compatibility to be integrated on the LNOI platform with low loss [4]. To date, almost all building blocks for a complete photonic system have been realized on the LNOI platform with outstanding performance except one—photodetectors.

Photodetectors that convert high-speed optical signals into the electrical domain are essential components in optical communication networks and microwave photonics systems. Conventionally, output optical signals from a photonic system are fiber coupled into a discrete photodetector. This, however, introduces additional loss and is not compatible with the need for fully integrated chip-scale photonic solutions. In the past years, various efforts on integrated photodetectors on non-native substrates have focused on platforms including silicon and silicon nitride [5,6], and bandwidths approaching 70 GHz have been reported [7]. An early attempt was made on integrating photodiodes on LN waveguides using GaAs [8], and one demonstration of an integrated silicon photodetector on LNOI with 10-MHz bandwidth for visible wavelengths was made [9].

Here, we advance the LNOI platform's functionalities by demonstrating heterogeneously integrated modified uni-traveling

carrier (MUTC) photodiodes (PDs) on thin-film LN (TFLN) that achieve a record-high bandwidth of all reported heterogeneously integrated PDs on non-native substrates to date. We use an MUTC structure with optimized thicknesses of the depleted and undepleted absorbers based on InGaAs/InP, which enables an 80-GHz bandwidth, low dark current of 3 nA, high internal responsivity of 0.6 A/W, and ability to detect a 40-Gbit/s data stream without additional electronic amplifiers.

2. DEVICE DESIGN AND FABRICATION

Figure 1(b) shows the MUTC PD layers that were grown as a p-down structure lattice-matched on a semi-insulating InP substrate. In this design, the thicknesses of the InGaAs absorber layers were optimized to maximize the carrier transit time-limited bandwidth. To this end, we calculated the frequency response of the sum of the three following current contributions: electron diffusion current, hole drift current, and electron drift current. They can be expressed as integral functions with respect to positions of carriers spanning the region from the absorber to the drift layer [10]. The ratio of the depleted absorber and the undepleted absorber was then chosen to maximize the carrier transit time-limited bandwidth of the photodiode. Figure 2(a) shows the calculation result using the parameters in Table 1. With a fixed total absorber thickness of 250 nm, we found a maximum of 167 GHz for a 50-nm undepleted absorber and a 200-nm depleted absorber. A 50-nm cliff layer made of moderately n-type-doped InP is added to reduce the space charge effect [11]. Since InGaAs and InP have a difference in band gap, InAlGaAs with a 0.86-eV band gap was chosen as the bandgap-grading layer material. Grading layers on both the n-side and the p-side help carriers to overcome the band discontinuities.

As shown in Fig. 1(a) and in contrast to our previous work [5], we designed a structure that results in n down after bonding with the following benefits: the InP n-contact layer is transparent at the operating wavelength 1550 nm; a low sheet resistance in the contact layer can be achieved since high n-type doping levels ($>10^{19}$ cm^{-3}) can easily be reached in InP together with high electron mobility; formation of n-metal contacts with low contact resistance; and keeping p-type InGaAs as the top contact layer without compromising the responsivity. Although the layer structure was specifically designed for 1550 nm, we expect that the PD has a broad working wavelength range that is ultimately limited by the bandgaps of the highly doped InP contact layer (920 nm) and the absorber InGaAs (1650 nm).

Figure 1(c) shows a schematic of the TFLN waveguide which was optimized for photodiode integration. The total thickness of LN is 600 nm with the waveguide height being 250 nm. We deposited SiO_2 on top of the trench waveguides followed by chemical-mechanical polishing (CMP) to improve surface flatness. The total thickness of the SiO_2 layer after CMP is 100 nm on top of the waveguide, which is optimal for both bonding and evanescent light input coupling from the waveguide into the PD. With this standard TFLN platform, other optical devices, such as ring resonators and modulators can be simultaneously fabricated on the same chip as shown in Fig. 1(e).

Table 1. Bandwidth Calculation Parameters

Parameter	Value
Thermionic emission velocity in InGaAs	2.5×10^5 m/s
Hole saturation velocity	0.45×10^5 m/s
Electron velocity in InGaAs and InP	1×10^5 m/s
Electron mobility in p-type InGaAs	0.5 $m^2/(V \cdot s)$
Electron diffusivity in p-type InGaAs	1.3×10^{-2} m^2/s
External load resistance	50 Ω
Series resistance	5 Ω

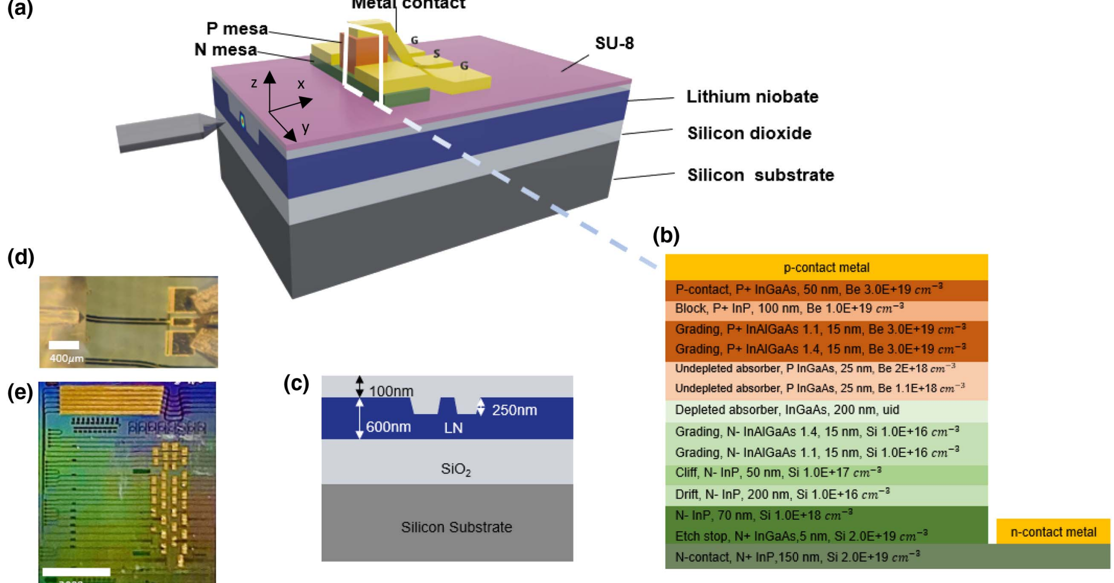

Fig. 1. MUTC PDs integrated on TFLN. (a) Structural illustration. (b) Epitaxial structure of the n-down PD. (c) TFLN waveguide cross section. (d) Microscope image of a device under test with a lensed fiber and a radio frequency probe. (e) Microscope image of chip with integrated PDs.

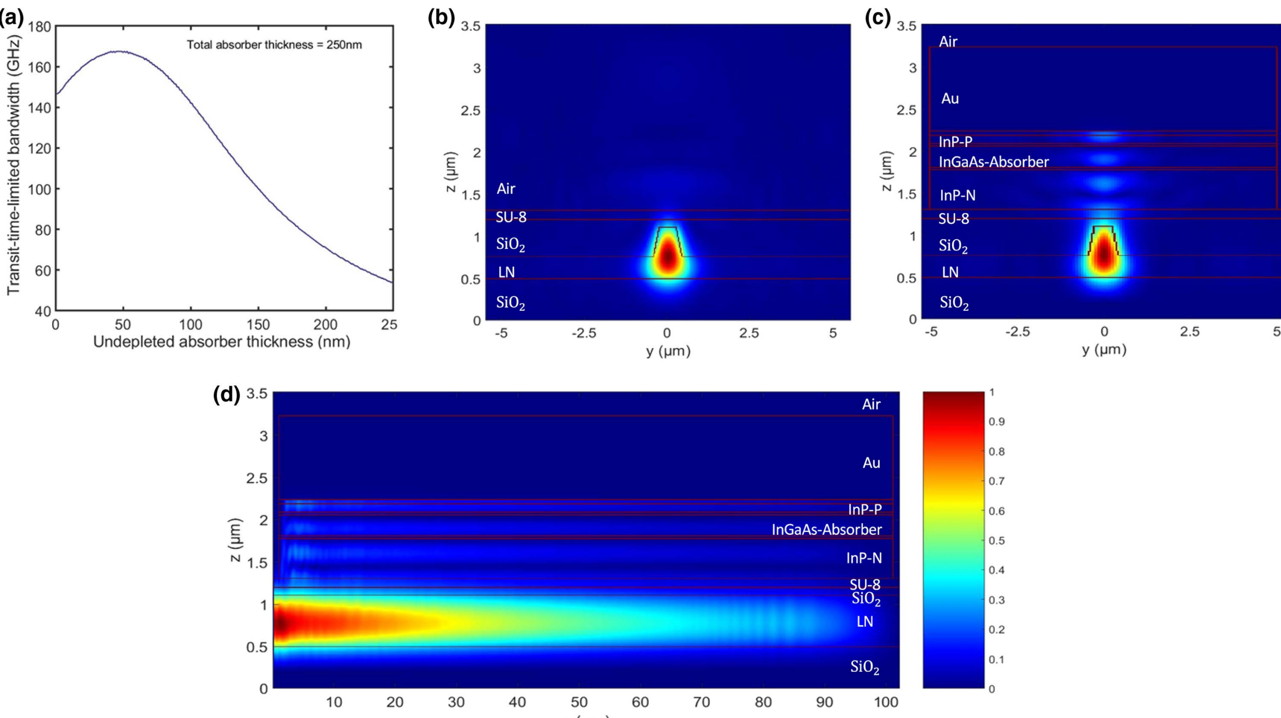

Fig. 2. Device simulations. (a) Calculation of transit time-limited bandwidth versus undepleted absorber thickness with total absorber thickness of 250 nm and a fixed drift layer thickness of 200 nm. Optical simulations of E-field magnitude: (b) yz cross section at $x = 0$ μm (passive waveguide), (c) yz cross section at $x = 5$ μm (PD), and (d) zx cross section at $y = 0$ μm.

Photodiodes were fabricated by first bonding a 4-mm × 8-mm InGaAs/InP MUTC wafer die on TFLN waveguides covering the area where PDs were then fabricated. With sufficient margins on all sides, the alignment accuracy for this step was 500 μm. We used SU-8 as the adhesive bonding agent. The thickness of SU-8 was controlled by spin coating speed and designed to be 100 nm for a high optical coupling efficiency. Figures 2(b)–2(d) show a simulation of the light coupling from the LN waveguide into the photodiode. SU-8 was both UV and high temperature cured to achieve higher stability. After a 40-min outgas, the PD epitaxial material die and the LNOI chip were brought in contact and cured at 130°C under 10 psi for 60 min. The InP substrate of the III–V photodiode die was removed after bonding using wet etch (HCl). For the n-mesa fabrication, we used inductively coupled plasma reactive ion etching (Cl_2 and N_2) followed by a short selective wet etching (HCl) to expose the InP contact layer. The combination of the two methods allowed us to largely avoid undercut which can be detrimental for small mesa areas, whereas, ensuring to stop the etching above the InP. The p-mesa formation was performed by wet etching (H_3PO_2 and HCl). We fabricated PDs with the following active areas (width in y × length in x): 10 μm × 10 μm, 20 μm × 10 μm, 15 μm × 20 μm, 20 μm × 30 μm, and 20 μm × 50 μm. TFLN waveguides outside the bonding area were protected by photoresist during the fabrication process. An air-bridge structure was adopted to connect the metal on top of an n mesa and a p mesa to the ground-signal-ground (GSG) radio frequency (RF) pads. Those RF pads were designed to yield a characteristic impedance of 50 Ω.

3. DEVICE CHARACTERIZATION

A. DC Measurements

Dark current is an important figure of merit for PDs as it is one of the major sources for noise. The fact that the low dark current of our MUTC PD on a TFLN of 3 nA [Fig. 3(a)] is comparable to or lower than the dark current from similar PDs on a native substrate [12], indicates that the integration process did not degrade the performance.

The responsivity of the photodetectors was measured at 1550 nm by edge-coupling light into the TFLN waveguides. The external responsivity of the PDs was calculated by dividing the photocurrent by the optical power at the lensed fiber tip (measured by an optical power meter). For a 10-μm × 10-μm-sized photodiode, the external responsivity was 0.2 A/W. It should be mentioned that external responsivity is significantly affected by the fiber-to-waveguide coupling loss and does not reflect device performance well in this integration scheme. Thus, internal responsivity was characterized by investigating the ratio of photocurrent and the light coupled into waveguides. The average fiber-to-waveguide coupling loss was 5 dB. The loss was measured on a straight waveguide with a visibly good facet on the same chip using a conventional fiber-to-waveguide-to-fiber setup. This coupling loss measurement also agrees with the simulation result using the lumerical finite difference eigenmode to calculate mode overlap between the fiber mode and the transverse electric mode in the TFLN waveguide. It should be noted that we did not use an antireflection coating. With taking coupling loss into account, the internal responsivity of a 10 μm × 10 μm device is 0.6 A/W which agrees with

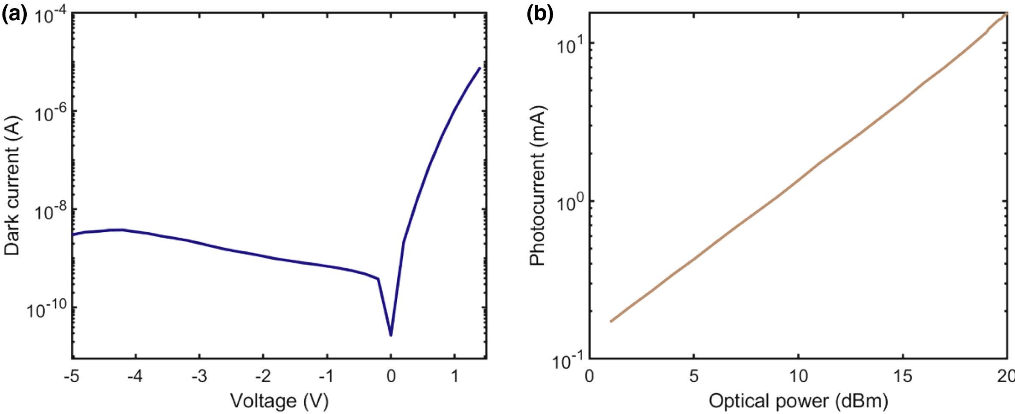

Fig. 3. DC measurements of MUTC photodiodes integrated on thin-film LN platform. (a) Dark current characteristics of a 1400-μm^2 device. (b) Measurement of photocurrent versus optical power (measured at fiber tip) of a 600-μm^2 device.

optical simulation using the lumerical FDTD module. The responsivities for PDs with areas of 20 μm × 10 μm, 15 μm × 20 μm, 20 μm × 30 μm, and 20 μm × 50 μm are 0.17, 0.24, 0.52, and 0.4 A/W, respectively. It should be mentioned that we diced the waveguide facets along the edge of the TFLN chip after photodiode integration, and there was visible nonuniformity across different facets. The fact that facet loss varies across different waveguides can explain the spreading of the measured responsivity data.

We also measured photocurrent versus optical power on a 20-μm wide and 30 μm-long PD. As shown in Fig. 3(b), the photocurrent was linear for input powers as high as 20 dBm.

B. Frequency Response

The 3-dB bandwidth was measured by a heterodyne setup. Two distributed feedback lasers with wavelengths near 1550 nm were used to generate a frequency tunable optical signal with near 100% modulation depth. The frequency of the beat signal is controlled by thermally tuning the wavelength of one laser, whereas the other laser remains at one stable wavelength. This optical signal was then directed to an erbium-doped fiber amplifier (EDFA) followed by a variable optical attenuator to control the amplitude of the optical signal. A single-mode tapered fiber was used to couple light into the TFLN waveguide. The fiber-to-waveguide alignment was performed using a six-axial stage. A GSG RF probe was used to extract the photocurrent by probing at the designed RF metal pads [Fig. 1(d)]. A semirigid coaxial cable was used to connect the RF probe with the bias tee. The RF signal was detected using a calibrated 50-Ω RF power meter with frequency range from DC to 110 GHz. The losses of the RF probe, semirigid coaxial cable, and bias tee were determined with a 110-GHz network analyzer and then subtracted from the measured data.

Figure 4(a) shows the bandwidth measurements of a 100-μm^2 PD at photocurrents of 0.5 and 1 mA at the same 3-V reverse bias. The 3-dB bandwidth of 80 GHz did not change with different photocurrents, and the output RF power from the photodiode matches the expectation. Figure 4(b) shows the bandwidth measurement results of the photodetectors with 100, 200, 600, and 1000-μm^2 device areas. Photocurrent was kept the same during measurements by adjusting the fiber alignment and the polarization of the optical signal controlled by a fiber polarization controller. The highest 3-dB bandwidth of 80 GHz was achieved with the 100-μm^2 photodetector, and the 3-dB bandwidth decreased as the device active area increased. If the PD is significantly shorter than the electrical signal wavelength, the photodetector can be treated as a lumped circuit element. Therefore, the resistance-capacitance (RC) time and carrier transit time are the two primary bandwidth limitations. Figure 4(c) shows the simulated transit time limit, the RC limit, and the 3-dB bandwidth for this epitaxial structure, and the measured bandwidth values agree well with the calculation. In this calculation, we use the calculated transit time-limited bandwidth of 167 GHz and a total resistance of 55 Ω (50-Ω external load and 5-Ω series resistance). Figure 4(d) shows the RF power at 48 GHz measured at different reverse biases. The maximum RF power was −1.9 dBm at 10 mA and 6.3 V. It should be mentioned that a higher reverse voltage led to PD failure at DC dissipated power of >70 mW. We expect that the high-power performance of the PD on LNOI can be further improved by flattening the absorption profile to avoid localized saturation [13].

C. Eye Diagram

Digital data detection performance of the photodetectors was characterized by an eye diagram measurement. A non-return-to-zero on–off keyed pseudorandom bit sequence (PRBS) data pattern was generated by a PRBS generator at 40 Gbit/s. Figure 5(a) illustrates our experimental setup. An external cavity laser provided the optical signal for a commercial 40-GHz modulator. The 550-mV peak-to-peak signal from the PRBS generator was fed into the modulator biased at its quadrature point. The optical signal then went through an EDFA, a variable optical attenuator, and an optical filter with a 1-nm passband before being coupled into the TFLN waveguides. The electrical signal was extracted by an RF probe and went through a semirigid cable, a bias tee, and a coaxial cable before entering the 50-GHz sampling oscilloscope for the readout. It is worth mentioning that our PD handled sufficient photocurrent and provided a high signal-to-noise ratio for the oscilloscope, so no additional RF amplifier to boost up the electrical signal was necessary in the measurement.

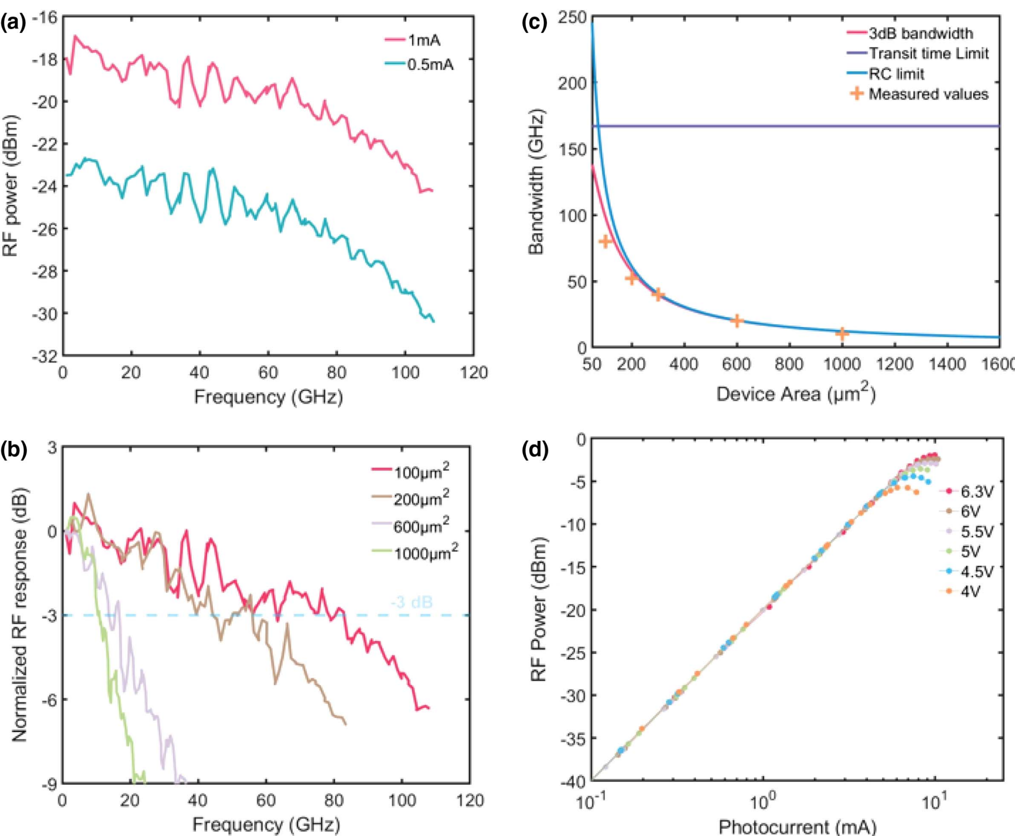

Fig. 4. AC measurements of MUTC photodiodes integrated on thin-film LN. (a) Frequency responses of a 100-μm² PD at different photocurrents. (b) Frequency responses of various sized photodiodes at 1-mA photocurrent and 3-V reverse bias. (c) Simulations and measurements of bandwidth for different device areas. (d) Measurement of RF power of a 300-μm² PD at 48 GHz at different reverse biases.

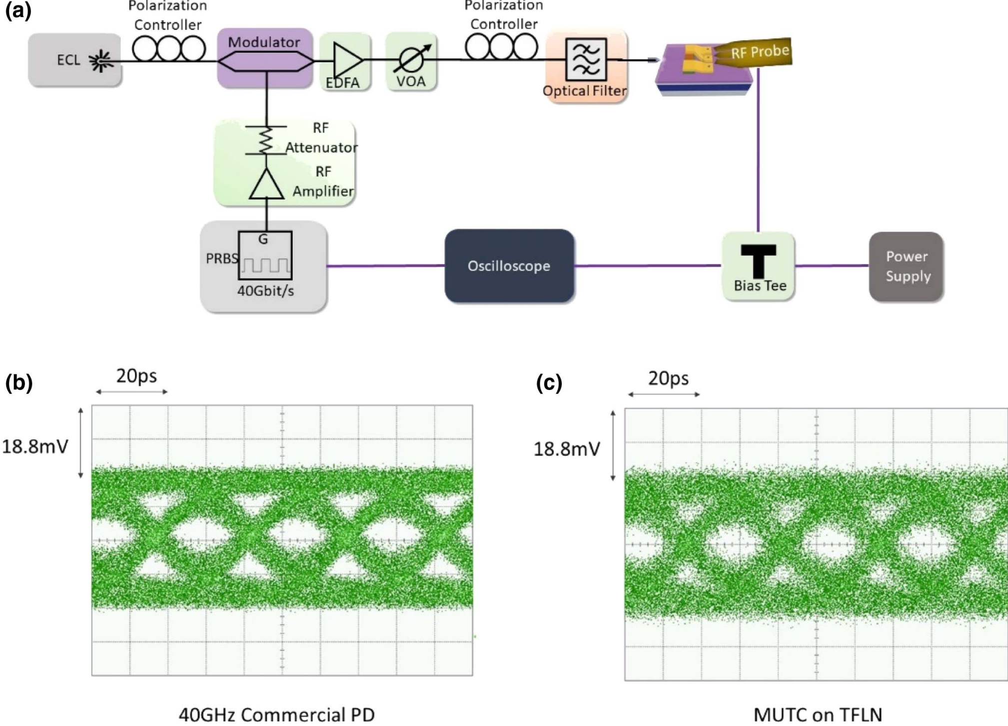

Fig. 5. Eye diagram measurement. (a) Measurement system setup. (b) Measured eye diagram for a commercial photodiode. (c) Measured eye diagram for an MUTC photodiode on TFLN with 200-μm² PD area.

We first measured the eye diagram of a commercial PD with a 40-GHz bandwidth shown in Fig. 5(b) as a reference. Figure 5(c) shows the measurement result of our 200-μm^2 PD with the measured 3-dB bandwidth of 52 GHz. It should be mentioned that the commercial PD was connected directly on the input port of the oscilloscope, whereas the on-chip measurement of our photodetector required additional RF parts that were not calibrated out from the eye diagram. Even with the extra loss in the system, our photodetector performs similarly to the commercial PD. The clear open eye diagram proves the high-speed performance of our photodetector and demonstrates its capability for digital communication applications.

4. SUMMARY

In conclusion, we designed and fabricated MUTC photodiodes on TFLN waveguides. The internal responsivity for a high-speed photodiode with an 80-GHz bandwidth was 0.6 A/W. The dark current was as low as 3 nA. The fabrication process of our MUTC photodiodes was fully compatible with modulators and ring resonators on the same wafer. With excellent performance, our integrated MUTC photodiode could enable high-performance photonic integrated circuits on the LNOI platform.

Funding. National Science Foundation (2023775); Air Force Office of Scientific Research (FA 9550-17-1-0071); Defense Advanced Research Projects Agency (HR0011-20-C-0137).

Acknowledgment. The views, opinions, and/or findings expressed are those of the author(s) and should not be interpreted as representing the official views or policies of the Department of Defense or the U.S. Government. The authors from University of Virginia also acknowledge the Multidisciplinary University Research Initiative (MURI) program through the AFOSR, monitored by Dr. G. S. Pomrenke.

Disclosures. The authors declare no conflicts of interest.

Data Availability. All relevant data are available from the corresponding author upon request.

REFERENCES

1. M. Zhang, C. Wang, R. Cheng, A. Shams-Ansari, and M. Lončar, “Monolithic ultra-high-*Q* lithium niobate microring resonator,” Optica **4**, 1536–1537 (2017).
2. C. Wang, M. Zhang, X. Chen, M. Bertrand, A. Shams-Ansari, S. Chandrasekhar, P. Winzer, and M. Lončar, “Integrated lithium niobate electro-optic modulators operating at CMOS-compatible voltages,” Nature **562**, 101–104 (2018).
3. D. Zhu, L. Shao, M. Yu, R. Cheng, B. Desiatov, C. J. Xin, Y. Hu, J. Holzgrafe, S. Ghosh, A. Shams-Ansari, E. Puma, N. Sinclair, C. Reimer, M. Zhang, and M. Lončar, “Integrated photonics on thin-film lithium niobate,” Adv. Opt. Photon. **13**, 242–352 (2021).
4. A. Shams-Ansari, D. Renaud, R. Cheng, L. Shao, L. He, D. Zhu, M. Yu, H. Grant, L. Johansson, M. Zhang, and M. Lončar, “Electrically pumped laser transmitter integrated on thin-film lithium niobate,” Optica **9**, 408–411 (2022).
5. Q. Yu, J. Gao, N. Ye, B. Chen, K. Sun, L. Xie, K. Srinivasan, M. Zervas, G. Navickaite, M. Geiselmann, and A. Beling, “Heterogeneous photodiodes on silicon nitride waveguides,” Opt. Express **28**, 14824–14830 (2020).
6. D. Maes, G. Roelkens, M. Zaknoune, C. O. de Beeck, S. Poelman, M. Billet, M. Muneeb, S. Lemey, E. Peytavit, and B. Kuyken, “Heterogeneous integration of uni-travelling-carrier photodiodes using micro-transfer-printing on a silicon-nitride platform,” in *Conference on Lasers and Electro-Optics Europe and European Quantum Electronics Conference* (2021), p. 1.
7. P. Tiwari, P. Wen, S. Mauthe, M. Baumann, B. I. Bitachon, H. Schmid, J. Leuthold, and K. E. Moselund, “Butt-coupled III-V photodetector monolithically integrated on soi with data reception at 50 Gbps OOK,” in *Optical Fiber Communication Conference* (2021), paper F2C.2.
8. A. Yi-Yan, W. K. Chan, T. J. Gmitter, L. T. Florez, J. L. Jackel, E. Yablonovitch, R. Bhat, and J. P. Harbison, “Grafted GaAs detectors on lithium niobite and glass waveguides,” IEEE Photon. Technol. Lett. **1**, 379–380 (1989).
9. B. Desiatov and M. Lončar, “Silicon photodetector for integrated lithium niobate photonics,” Appl. Phys. Lett. **115**, 121108 (2019).
10. T. Ishibashi, Y. Muramoto, T. Yoshimatsu, and H. Ito, “Unitraveling-carrier photodiodes for terahertz applications,” IEEE J. Sel. Top. Quantum Electron. **20**, 3804210 (2014).
11. A. Beling, X. Xie, and J. C. Campbell, “High-power, high-linearity photodiodes,” Optica **3**, 328–338 (2016).
12. Q. Li, K. Sun, K. Li, Q. Yu, P. Runge, W. Ebert, A. Beling, and J. C. Campbell, “High-power evanescently coupled waveguide MUTC photodiode with <105-GHz bandwidth,” J. Lightwave Technol. **35**, 4752–4757 (2017).
13. X. Xie, Q. Zhou, E. Norberg, M. Jacob-Mitos, Y. Chen, A. Ramaswamy, G. Fish, J. E. Bowers, J. Campbell, and A. Beling, “Heterogeneously integrated waveguide-coupled photodiodes on SOI with 12 dBm output power at 40 GHz,” in *Optical Fiber Communication Conference* (2015), paper Th5B.7.